

RESEARCH

Open Access



Application of in-situ gamma spectrometry for radiogenic heat production estimation in the Western Himalaya, Kohistan, and Karakoram in northern Pakistan

Muhammad Anees^{1*} , Jonas Kley¹, Bernd Leiss¹, David Hindle¹, Ali Abbas Wajid², Bianca Wagner¹, Mumtaz M. Shah³ and Elco Luijendijk⁴

*Correspondence:
muhammad.anees@stud.uni-goettingen.de

¹ Department of Structural Geology and Geodynamics, Geoscience Centre, Georg-August-Universität Göttingen, Göttingen, Germany

² Environmental Resources Management (ERM) GmbH, Frankfurt, Germany

³ Department of Earth Sciences, Quaid-i-Azam University Islamabad, Islamabad, Pakistan

⁴ Department of Earth Science, University of Bergen, Bergen, Norway

Abstract

The Himalaya, Kohistan, and Karakoram ranges comprise Proterozoic to Cenozoic crystalline complexes exposed in northern Pakistan. Numerous hot springs in the area indicate high subsurface temperatures, prompting a need to evaluate the local contribution of radiogenic heat to the general orogenic-related elevated geothermal gradients. The current study employed a portable gamma spectrometer to estimate the in-situ radiogenic heat production in the Nanga Parbat Massif, Kohistan–Ladakh batholith, and the Karakoram batholith. Heat production in the Nanga Parbat Massif is high, with a range from 0.2 to 10.8 μWm^{-3} and mean values of 4.6 ± 2.5 and 5.9 ± 1.9 μWm^{-3} for gneisses and granites, respectively. By contrast, the heat production is low in the Kohistan–Ladakh batholith, ranging from 0.1 to 3.1 μWm^{-3} , with the highest mean of 2.0 ± 0.5 μWm^{-3} in granites. The Karakoram batholith shows a large variation in heat production, with values ranging from 0.4 to 20.3 μWm^{-3} and the highest mean of 8.4 ± 8.3 μWm^{-3} in granites. The in-situ radiogenic heat production values vary in different ranges and represent considerably higher values than those previously used for the thermal modeling of Himalaya. A conductive 1D thermal model suggests 93–108 °C hotter geotherms, respectively, at 10 and 20 km depths due to the thick heat-producing layer in the upper crust, resulting in a surface heat flow of 103 mWm^{-2} . The present study provides first-order radiogenic heat production constraints for developing a thermal model for geothermal assessment.

Keywords: Radiogenic heat production, Gamma spectrometry, Thermal model, Himalaya, Karakoram, Pakistan

Introduction

Radioactive decay of radioelements, i.e., Uranium, Thorium, and Potassium (^{238}U , ^{235}U , ^{232}Th , and ^{40}K), is one of the most important heat generation processes in the Earth's crust. The information about variations in magnitude and distribution of radioelements is vital for geothermal assessments as it can significantly impact regional and local heat flow (Jaupart et al. 2016). Among crustal rocks, granitoids tend to have higher

concentrations of radioelements and can enhance the geothermal gradient, which is favorable for geothermal exploration and development (Gnojek et al. 2018; McCay & Younger 2017). Crustal evolution processes, such as orogeny, subduction, magmatic differentiation, etc., which form large crystalline complexes of granitoids, are responsible for the heterogeneous distribution of radioelements (Artemieva et al. 2017). Thus, it is essential to estimate the variation in the distribution of radioelements across the various lithological units to constrain their contribution to the heat flow and its potential geothermal implications.

The Himalayas, Kohistan, and Karakoram Ranges collectively form the Tethyan collisional belt of the Indian and Eurasian plates in north Pakistan and surrounding regions (Kazmi and Jan 1997). These ranges host hydrothermally active zones along and in the vicinity of tectonic sutures and intraplate thrust faults (e.g., Main Karakorum Thrust, Main Mantle Thrust, and Main Boundary Thrust (Bakht 2000; Fig. 1). Previous studies have suggested various mechanisms for the origin of hydrothermal activity, including radioactive decay, shear heating along faults, residual heat from younger plutonic intrusions, plastic deformation, metamorphic heat due to tectonic collision, and rapid exhumation (Butler et al. 1997; Craw et al. 1997; Hochstein and Regenauer-Lieb 1998; Chamberlain et al. 2002; Zaigham et al. 2009). The lack of borehole data hinders

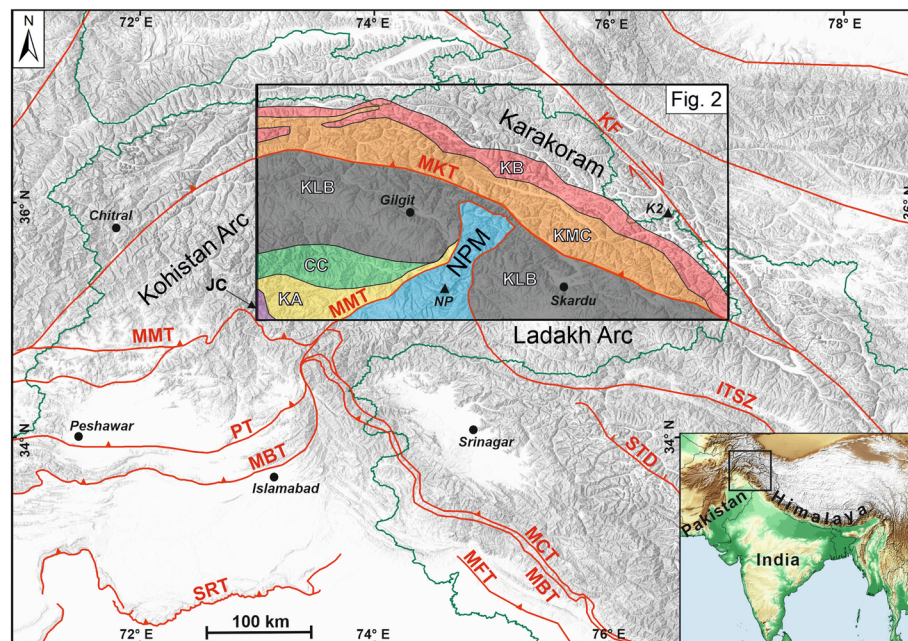


Fig. 1 Generalized tectonic map of north Pakistan (overlaid on a hill-shade terrain model) showing regional faults/sutures in the western Himalaya, Kohistan, and Karakoram. The political boundaries are shown with thin green lines. The black square in the inset figure (bottom right) shows the geographic location of Fig. 1 in South Asia. The black box in the center shows the spatial extent of Fig. 2 (study area) and regional geologic units of the Indian plate (NPM—Nanga Parbat Massif), Kohistan–Ladakh arcs (CC, JC, KA, KLB), and the Asian Plate (Karakoram—KB, KMC) (modified after Searle et al. 1999). CC Chilas Complex, ITSZ Indus–Tsangpo Suture Zone, JC Jijal Complex, KA Kamila Amphibolite, KB Karakoram Batholith, KF Karakoram Fault, KLB Kohistan–Ladakh batholith (and volcanics), KMC Karakoram Metamorphic Complex, MBT Main Boundary thrust, MCT/PT Main Central thrust/Panjtal thrust, MFT Main Frontal thrust, MKT Main Karakorum thrust, MMT Main Mantle thrust, NP Nanga Parbat, SRT Salt Range thrust, STD South Tibet detachment

understanding the subsurface geothermal gradient and heat flow. Although some studies have numerically modeled subsurface geotherms in the context of exhumation and regional metamorphism while assuming standard petrophysical (heat production and thermal conductivity) values (Craw et al. 1994; Treloar 1997), the magnitude and variations of heat produced in the crust due to radioactive decay still need to be estimated for reliable geothermal modeling.

In this study, we aim to estimate the radiogenic heat production in prevailing crystalline lithologies using the concentration of radioelements (U, Th, and K) measured with a field gamma spectrometer. Furthermore, we examine the intrinsic variations in radiogenic heat production values associated with different rock types to understand the factors controlling these variations and their possible implications on crustal geotherms using a one-dimensional thermal model. The results of this study will provide better constraints for future thermal modeling studies to explore the geothermal potential of the study area.

Tectonic settings and geology

Northern Pakistan is tectonically subdivided from the north to the south into the Karakoram block (Eurasian plate), Kohistan (-Ladakh) arc, and the Himalayas (Indian plate) (Kazmi and Jan 1997). The Kohistan arc (largely intra-oceanic) got sandwiched between the Eurasian and Indian plates due to the closing of neo-Tethys along two suture zones and their subsequent collision (Tahirkheli 1979). These sutures are the Main Karakoram Thrust (MKT), which marks the boundary between the Karakoram and Kohistan, and the Main Mantle Thrust (MMT), which marks the suture between the Kohistan arc and Himalayas (Gansser 1980; Kazmi et al. 1984).

The study area forms part of three tectonic domains, i.e., the Nanga Parbat Massif of the Himalaya, Kohistan (and Ladakh) batholith of the Kohistan (-Ladakh) arc, and Karakoram batholith of the Karakoram block (Fig. 1). The following section includes further details about important tectonic features and geological units related to our study area.

Nanga Parbat Massif

The Nanga Parbat Massif is the northernmost part of the Himalayas in Pakistan, where the Proterozoic Indian basement crust is exposed up to an elevation of ~8 km (Fig. 1). The region exhibited substantial uplift of up to 30 km during Himalayan orogeny, forming an N-S striking syntaxis thrusting onto the Kohistan arc (Butler et al. 1989; Zeitler et al. 1993). It comprises an Archean to mid-Proterozoic migmatitic-quartzofeldspathic, basement, gneissic core, flanked by late Proterozoic calcareous and pelitic gneisses and amphibolites, with late Cenozoic pegmatitic and leucogranitic intrusions (Butler and Prior 1988; Zeitler et al. 1989). The metamorphic grade increases from amphibolite along the margins to granulite towards the massif's core.

The basement rock units of the massif, also collectively termed the Nanga Parbat Group, are subdivided into Iskere Gneiss, Shengus Gneiss, and Haramosh Schist (Madin et al. 1989; Tahirkheli 1983). The Iskere Gneiss, with zircons ranging in age up to 1.85 Ga, comprises coarse-grained biotite orthogneisses with minor biotite schist, amphibolite, and calc-silicates (Zeitler et al. 1989). The Shengus Gneiss incorporates laminated fine-grained amphibolite-grade paragneisses of pelitic and psammitic origin, interlayered

with calc-silicates and amphibolites (Madin 1986). The Haramosh Schist comprises biotite schist and gneiss of amphibolite grade with subordinate marble and calc-silicates.

The Miocene age intrusions resulted from late Cenozoic uplift and partial melting, distributed in the older rocks in the form of migmatites, small granitic plutons ($\sim 1 \text{ km}^2$), leucogranite, pegmatite dikes, and cordierite-bearing veins (Zeitler et al. 1993). The dikes and veins are 1 cm to 50 m in thick and consist of quartz, feldspar, muscovite, biotite, tourmaline, and garnets.

Kohistan–Ladakh arc

The Kohistan–Ladakh arc is a ca. 700 km long, mainly E–W trending island-arc terrane separated by the Nanga Parbat Massif into the Kohistan arc in the west and the Ladakh arc to the east (Tahirikheli 1979). The Kohistan arc comprises a complete crustal section of the mantle to the uppermost crustal rocks. In contrast, the Ladakh arc predominantly comprises upper crustal volcanic and plutonic rocks (Treloar et al. 1990).

The Kohistan Island arc consists of ca. 30 km thick igneous and sedimentary rock sequences of Cretaceous age subdivided into five following parts (Fig. 1; Petterson 2010);

- (1) The Jijal complex, towards the north of the MMT, is composed of ultramafic to mafic rocks (including harzburgites, upper granulite facies garnet granulites, websterites, and pyroxenites) and forms the lower and southernmost part.
- (2) The Kamilia Amphibolites are exposed towards the north of the Jijal complex and consist of metavolcanics (basalts and basaltic andesites) and metaplutonics (basalts and basaltic andesites).
- (3) The Chilas complex comprises basic–ultrabasic plutonic gabbro-norite rocks.
- (4) The Jaglot group, a volcanic–metasedimentary group, has lithologies, such as metasandstones, carbonates, siltstones, mudstones, and turbidites with local metabasalt, andesite, and rhyolite volcanic rocks.
- (5) The Kohistan batholith is exposed north of the Jaglot group, intrusive into the Chalt volcanic group, and overlain by Yasin volcanoclastics towards the north until the MKT (Petterson and Treloar 2004).

The Kohistan batholith is a mid-upper crustal plutonic unit formed by the magmatic event (spanning ca. 86 Ma) in an intra-oceanic subduction setting before the India–Eurasia collision (Petterson 2010). It is a composite of gabbro-diorites, trondjemites (Matum Das pluton), granites, and leucogranite sills and dikes (Hanzel, Jutal and Confluence granite) (Petterson et al. 1993; Treloar et al. 1996). Three distinct growth phases have been identified, i.e., deformed plutons (ca. 102 Ma), which are intruded by undeformed gabbros, granites, and diorites, cut by late granite sheets (50–26 Ma) (Petterson and Windley 1985). The Ladakh batholith (the eastern equivalent of the Kohistan batholith) is predominantly composed of biotite–hornblende granites, tonalites, diorites, gabbros, and norites. It also includes volcanic units primarily exposed in its eastern parts (Singh 1993).

Karakoram block

The Karakoram block forms the southern margin of the Eurasian plate. It is subdivided (from north to south) into the Northern Karakoram Basin, Karakoram Batholith, and Karakoram Metamorphic Complex (Searle and Khan 1996). The northern Karakoram represents a back-arc sedimentary basin with Palaeozoic carbonates and clastic

sedimentary rock deposits that extend northward towards the southern Pamir (Palin et al. 2012).

The Karakoram Batholith is an E–W trending, 600 km long and up to 30 km wide axial batholith that separates the northern sedimentary sequence from the southern metamorphic complex (Fig. 1; Crawford and Searle 1992; Searle et al. 1989). The batholith consists of plutonic units of different ages, chemical and mineralogical composition, and tectonometamorphic history (Debon et al. 1987). It predominantly comprises Cretaceous I-type granodiorites and diorites intruded by Cenozoic leucogranites (Searle and Tirrul 1991). The lithological units exposed in the western and central parts comprise sub-alkaline and calc–alkaline subduction-related Andean-type pre-Himalayan granitoids (Hunza plutonic unit) of mid-Cretaceous age (Crawford and Searle 1992). The eastern part consists of exhumation-related post-Himalayan leucogranites and monzogranites (Baltoro plutonic unit, Kande plutonic complex) to syenite of Miocene age (Searle et al. 2010; Villa et al. 1996).

The Karakoram Metamorphic Complex contains kyanite to sillimanite grade schists, paragneisses, amphibolites, and interlayered marbles and pegmatites (Bertrand et al. 1988; Searle et al. 1989). The high-grade gneisses of the Karakoram metamorphic complex are in thrust contact with low-grade metavolcanics of the Kohistan along the MKT (Fig. 1; Searle et al. 1989). The Dassu gneiss exposed in the Shigar valley forms a lower crustal dome composed of felsic orthogneiss containing zircons of Precambrian inheritance and intruded by leucogranite bodies formed by partially melting in Pliocene time (Searle et al. 1989).

Materials and methods

In-situ gamma spectrometry

We used a portable gamma spectrometer called Exploranium GR-135G Plus (SAIC, Canada) to collect in-situ radioelement concentration data in the field. The instrument employs a Sodium Iodide (Thallium) 38×57 mm detector, which can detect radionuclides with a gamma energy detection range from 0 to 3.0 MeV and uses 256 channels for spectral analysis (SAIC Exploranium 2006). The instrument was calibrated every 24 h with a Cesium 137 calibration source for greater accuracy. We acquired our data using the assay mode, which spectrally analyzes the gamma energies and calculates the concentrations of U (ppm), Th (ppm), and K (wt %) using the calibration coefficients stored in its memory. The instrument's precision (according to manufacturer) in assay mode for 120 s count time for a sample (with 2% K, 2 ppm U, and 8 ppm Th) in typical background is $\pm 0.35\%$, ± 1.5 ppm, ± 2.6 ppm for K, U and Th, respectively (SAIC Exploranium 2006).

We selected a measurement time of 300 s to obtain stable spectra. When in direct contact with an outcrop, the instrument collects the gamma rays emitted from 15 to 25 cm depth (depending upon density) within a 1 m circular disc. The instrument applies stripping and background corrections on the acquired spectrum and displays the concentrations of U and Th in ppm and K in wt % as output.

Data acquisition

The concentration of the radiogenic elements (U, Th, K) is commonly high in felsic rocks composing the upper continental crust (Jaupart and Mareschal 2005); therefore, we

primarily targeted the granitoids, gneisses, and leucogranite intrusions (Fig. 2). We collected radioelement data from 158 readily accessible roadside fresh outcrops along the valleys. In the Nanga Parbat massif, the Raikot valley, the Astore, and Skardu roads provide access to Proterozoic basement rocks (including migmatites) with young intrusive dikes (of centimeters-to-meters thickness) along shear zones (Fig. 3b–e).

In the Gilgit and Ghizer valleys, the diorites (with varying composition), volcanogenic metasediments, and a few granitic outcrops represent the Kohistan batholith (Fig. 3h). The readings for the Ladakh batholith are taken from the granites, granodiorites, and gneisses from the sections exposed around the Skardu and Khaplu cities in the north-eastern part of the study area (Fig. 2).

The data from the Karakoram batholith and metamorphic complex is acquired from western, central, and eastern Karakoram, corresponding to the Hunza, Shigar, Hushe, and Saltoro valleys. In Hunza valley, Hunza plutonic complex and Sumayar leucogranite comprise gneiss, granodiorites, diorites, granite, leucogranites and pegmatites (Fig. 3i). Felsic gneisses (with pegmatites) of the Dassu gneissic dome and the syenitic pluton of Hemasil are sampled from upper Shigar Valley. In the Hushe and Saltoro valleys, the dioritic gneiss of the Hushe complex and hornblende monogranites of the Kande pluton (comprising the southern part of the Baltoro plutonic unit) represent the easternmost sampled locations of the Karakoram batholith for this study (Fig. 2).

During the field campaign, several hot spring sites (some with boiling temperatures) and alteration zones (active and fossil zones with H₂S smell and sulphurised rocks) were observed, as shown in Figs. 2 and 3f, g. These hydrothermal zones are mostly located in the vicinity of suture zones and faults, such as in the Raikot, Hunza, Shigar, and Saltoro valleys (Fig. 2).

Data corrections and validation

Data acquisition using a portable gamma spectrometer ideally requires a flat section of outcrop with minimal topographical features to meet 2 π steradians or half space

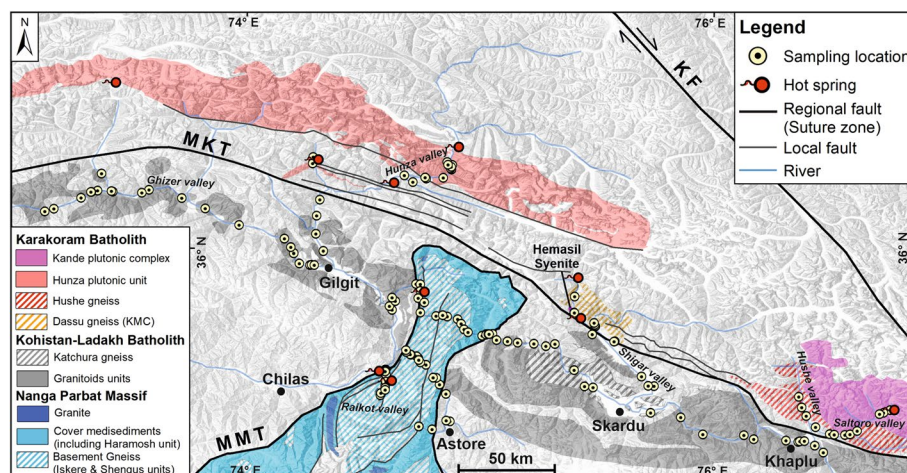


Fig. 2 Map showing sampling locations, active hot springs, and the geological units sampled in our study (redrawn after Madin et al. 1989; Schneider et al. 1999, Searle and Khan 1996). Abbreviations are the same as in Fig. 1

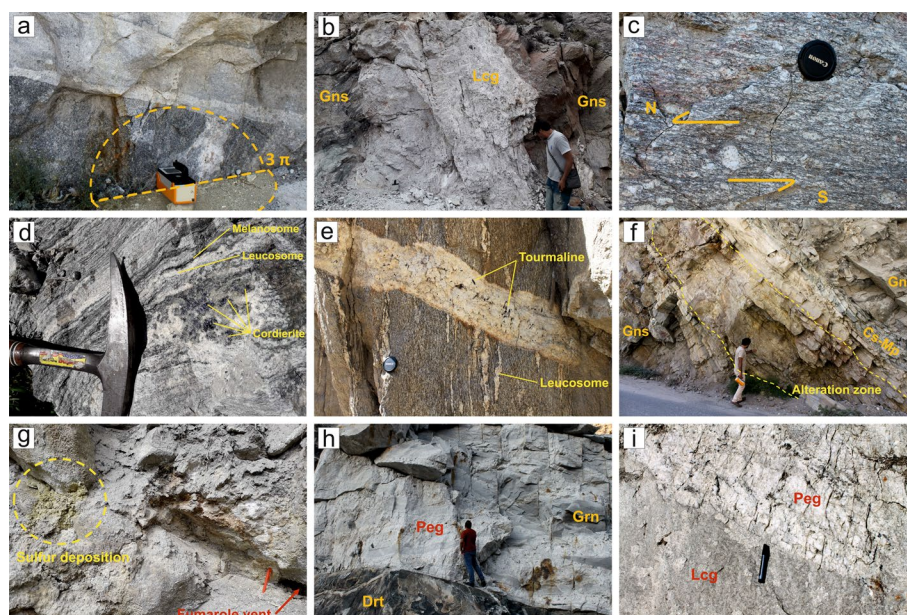


Fig. 3 **a** Field gamma spectrometer acquiring U–Th–K data from an outcrop with 3π geometry. **b** Leucogranite (Lcg) dike (with euhedral tourmaline crystals) intruding basement gneiss (Gns) along the Raikot shear zone in the Nanga Parbat Massif (NPM). **c** Sheared augen gneiss showing shear deformation in NPM along the Raikot fault. **d** Cordierite in the migmatitic gneiss display HT–LP conditions in core of the Nanga Parbat during exhumation. **e** Tourmaline bearing pegmatite dike cross cutting the gneissic fabric in NPM. **f** Alteration zone (with sulfide smell) showing precipitation of secondary minerals in calc–silicate metapelite (Cs–Mp) along Astore road in NPM. **g** Hydrothermal deposition of sulfur around the hot spring site at Murtazabad (north of MKT) in the Karakoram metamorphic complex. **h** Pegmatite (Peg; with garnet and tourmaline) intruding granite (Grs) which is intruding diorite (Drt) of the Kohistan–Ladakh batholith at the confluence of the Indus and Gilgit rivers (i) contact between leucogranite (Lcg) and two-mica Pegmatite (Peg) at the southern edge of the Karakoram batholith along Nagar valley

(flat) geometric condition between the instrument and the outcrop (McCay et al. 2014). However, finding an outcrop with a flat rock surface in the high-relief terrain is challenging, leading to gamma energy overestimation in valleys (Erdi-Krausz et al. 2003; McCay et al. 2014). Moreover, acquiring data along road outcrops (as is the case in the current study) means that each sampling point acquired additional gamma energy (from an area ranging between 2 and 3π steradians; Fig. 3a), leading up to a 50% overestimation in the concentrations of radioelements that needs to be corrected to obtain accurate values (McCay and Younger 2017).

We have applied a geometric correction to our data to overcome the overestimation due to possible geometric errors with the outcrop and the instrument. For this, at each sampling point, the average outcrop angle relative to the horizontal surface was noted, e.g., a completely vertical outcrop (with 3π geometry) was allotted a 90° angle while a flat space (or 2π geometry) horizontal outcrop with 0° angle and the rest plotting in between these two extremes (Fig. 3a). Based on these angles, we obtained correction factors ranging from 0.6667 to 1, i.e., for a 90° angle outcrop that got one-third overestimation, the data values were multiplied by 0.6667 to reduce the values by one-third (or 33.33%). In contrast, all data values from an outcrop with a 0° angle were multiplied by one as it required no reduction. Correction factors for outcrops

with angles between 0 and 90° are calculated using a similar linear relationship. In the end, all three values of radioelements are multiplied by their respective correction factors to obtain geometrically corrected values.

To remove the possible overestimation of data due to topography, we followed an approach similar to altitude correction in airborne gamma spectrometry while assuming the additional gamma influence only for the valleys that are <500 m wide (IAEA 1991). The intensity of gamma radiation from the far side of valleys, calculated from the attenuation coefficient in the air for ~2 MeV energies, exponentially decreases to ~50% at 130 m and ~25% at 260 m at STP conditions. Beyond 500 m, the intensity of gamma rays will be <10% of their original intensity and thus cannot significantly cause overestimation. The height and slope length ratio for the valley's far side is calculated up to 500 m distance from the sample location using a digital elevation model. The slope to height and intensity factors are multiplied by measured concentration values to calculate the overestimation from the opposite side of the valley, which was then subtracted from measured concentration values (Eq. 1):

$$C_{TC} = C_{GC} - \left(C_{GC} \times I_{(d)} \times \frac{H}{S} \right) \quad (1)$$

where C_{GC} is concentration U, Th, and K after geometric correction, C_{TC} is concentration after topographic correction, $I_{(d)}$ is the intensity of gamma radiation in the air at a specific distance from the source, H is the height attained at the far side of the valley against the slope length (S) at 500 m from the sampling location.

For quality control of our field data, we compared our data with a subset of 21 samples analyzed using a lab-based High Purity Germanium (HPGe) gamma spectrometer, which has a superior resolution (of 1.85 keV) compared to NaI detectors (Younis et al. 2022). The comparison shows a strong positive correlation in Th and K values with R^2 of 0.93 and 0.86, respectively (see Additional file 1). In the case of U, although the correlation is strong ($R^2 = 0.88$), there is an average of ~6 ppm overestimation. We believe disequilibrium in the U decay series is the most probable cause, which can occur due to leaching of daughter products and radon escape from the decay chain (Erdi-Krausz et al. 2003). In the laboratory, secular equilibrium is achieved by storing samples in sealed containers for at least a month; however, disequilibrium (particularly in the U series) in the field is unavoidable. Therefore, to overcome this, we performed regression based on the slope equation between the lab and field data to recalculate the U concentration and remove the effect of disequilibrium.

Reliability of in situ gamma spectrometry

The in-situ gamma spectrometry through portable devices offers greater flexibility, representative, and faster data collection than lab-based geochemical and gamma spectrometers. In addition, they offer firsthand information at a reconnaissance scale, marking regions of interest for the follow-up detailed investigations. However, inevitable tradeoffs need to be considered depending on the nature of the study area. In topographically challenging terrains, such as narrow valleys with high mountains, it is common to get the overestimation in concentrations of radioelements (McCay et al. 2014; Reinhart and Herrmann 2019).

These errors can be minimized by carefully documenting the geometric and topographic features at the sampling location during the field survey and applying suitable corrections.

Since the concentrations of Th and U are calculated by measuring the gamma radiations from their respective daughter products from respective series, the disequilibrium can provide false values of these elements. U is highly susceptible to disequilibrium due to the frequent mobility of parent radionuclides, such as Radium and Radon (Minty 1997). Weathering and groundwater can cause leaching in an oxidizing environment and concentration (precipitation) of soluble Radium (^{226}Ra) and U in a reducing environment, respectively, causing under and overestimation (Dickson 1985). Radon (^{222}Rn) in a gaseous state escapes from the source into the atmosphere through joints and fractures, affecting the concentration of ^{214}Bi , which is used to calculate U concentration. In low-lying landscapes, a buildup of denser ^{222}Rn close to the surface can result in overestimation of U (Minty and Wilford 2004). Therefore, comparing a subset of field data with a lab-based gamma spectrometer is recommended. In the case of good correlation, correcting a larger field data set is possible using the correlation slope between two data sets. However, one disadvantage of this technique is that it can also lead to underestimation at locations unaffected by U disequilibrium. Nonetheless, this method has been proven most effective in this study.

Radiogenic heat production

Radiogenic heat production (A) is calculated in μWm^{-3} using the following equation of Rybach (1988):

$$A = (9.52 C_U + 2.56 C_{Th} + 3.48 C_K) \times \rho \times 10^{-5} \quad (2)$$

where ρ is the density of the rock given in kg/m^3 , C_U , C_{Th} , and C_K is the concentration of Uranium (ppm), Thorium (ppm), and Potassium (wt %), respectively. The heat production constants in W/kg for U, Th, and K are 9.52, 2.56, and 3.48, respectively. They reflect the contribution of each of the radioelements to the radiogenic heat production, which is highest for Uranium, followed by Potassium and Thorium.

The densities were determined by hydrostatic weighing (buoyancy technique) on sample cubes as per the German industry standard (DIN 52102). The sample cubes were dried at 40 °C until mass consistency and then fully saturated with demineralized water for 24 h, after 24 h of vacuum in a desiccator. Subsequent measurements of the wet and buoyancy weight (by weighing with an under-floor balance while submerging the sample in demineralized water) allow the calculation of the effective porosity, bulk, and matrix density. We calculated bulk densities of 60 samples and used average values for similar rock types for field data against which lab density was unavailable.

Thermal modeling

For our temperature modeling, we solve a non-linear, steady state, one-dimensional conductive heat transfer equation of the form as

$$(k(u)u)' = q \quad (3)$$

where u is temperature, $k(u)$ is a temperature-dependent thermal conductivity, and q is radiogenic heat production. u , and q are both functions of depth.

Temperature-dependent thermal conductivity is modeled according to the suggestion of Jaupart et al. (2016). We also include a temperature-dependent radiative heat transfer component of thermal conductivity at temperatures $> 1000^\circ\text{K}$ (Jaupart and Mareschal 2005). The equations describing temperature-dependent thermal conductivity and radiative heat transfer are

$$k_u = 2.26 - \frac{618.251}{u} + k_o \cdot \left(\frac{355.576}{u} - 0.30247 \right) \quad (4)$$

$$k_r = 0.37e^{-9} \cdot u^3, u \geq 1000^\circ\text{K} \quad (5)$$

where k_o is the measured thermal conductivity of the rock under surface conditions, and k_r describes the effect of radiative heat transfer on thermal conductivity at high temperatures. Hence, for Eq. (3)

$$k(u) = k_u + k_r \quad (6)$$

We solve the equation with Dirichlet boundary conditions of fixed temperatures at the top and base of the lithosphere. Our model incorporates an arbitrary number of layers for which values of both k_o and q can be defined. To deal with abrupt changes in coefficients, we use a finite-difference scheme of “half station” type according to Hindle and Besson (2023) and references therein. We use a tri-diagonal matrix algorithm and a fixed-point iteration scheme to solve the non-linear problem.

Results

Our main targets in this study are crystalline rock units of the Nanga Parbat Massif (NPM), Kohistan–Ladakh batholith (KLB), and Karakoram Batholith (KB), ranging from granitoids and gneisses to metavolcanic units. Our results here focus on the broad classification of the rock units (granite, granodiorite, gneiss, schist, etc.) rather than mineralogical variation or petrogenesis (e.g., biotite granite, orthogneiss, metadiorite, etc.). Such details are compiled during fieldwork and attached to the Additional file 1. The results of this study are summarized in the following sections:

Radioelements concentration

The mean concentrations and standard deviation of U, Th, and K, along with Th/U and K/U ratios for different lithologies of NPM, KLB, and KB, are shown in Table 1.

The concentrations of radioelements in the NPM and KB range between 0.30–22.57 and 0.34–44.51 ppm for U, 0.66–86.17 and 1.96–154.00 ppm for Th, and 0.50–7.40% and 0.90–7.70% for K. In KLB, the concentrations of U, Th, and K values are comparatively low, ranging between 0.12–4.53 ppm, 0.89–23.88 ppm, and 0.08–4.51%, respectively. The mean concentrations of U, Th and K for the gneisses of NPM (8.78 ± 5.50 ppm, 30.42 ± 19.80 ppm, and $3.72\% \pm 0.97\%$, respectively) tend to be high compared to KB (4.70 ± 2.60 ppm, 16.47 ± 8.66 ppm, and $3.63\% \pm 0.95\%$, respectively) and KLB gneisses (2.73 ± 0.50 ppm, 13.54 ± 1.21 ppm, and $2.51\% \pm 0.38\%$, respectively). The granites of NPM and KB have higher mean U concentrations (16.94 ± 7.85 and 15.81 ± 18.10 ppm, respectively) than KLB granites (2.96 ± 1.01 ppm). However,

Table 1 Mean values of U (ppm), Th (ppm), and K (%), and Th/U and K/U ratios and their standard deviations for different lithologies from Nanga Parbat Massif, Kohistan–Ladakh and Karakoram batholiths

| Lithology | N | eU (ppm) | eTh (ppm) | eK (%) | Th/U | K/U (10 ⁴) |
|---------------------------|----|---------------|---------------|-------------|---------------|------------------------|
| Nanga Parbat Massif | | | | | | |
| Gneiss | 36 | 8.78 ± 5.50 | 30.42 ± 19.80 | 3.72 ± 0.97 | 3.97 ± 1.80 | 0.61 ± 0.35 |
| Pegmatite | 7 | 8.54 ± 5.33 | 12.35 ± 6.93 | 4.28 ± 1.50 | 1.71 ± 1.03 | 0.74 ± 0.53 |
| Schist | 5 | 2.38 ± 1.27 | 9.05 ± 5.41 | 1.78 ± 0.85 | 3.55 ± 0.90 | 0.85 ± 0.37 |
| Granite | 3 | 16.94 ± 7.85 | 20.70 ± 6.36 | 4.22 ± 0.65 | 1.55 ± 1.14 | 0.29 ± 0.15 |
| Psammite | 2 | 0.30 ± 0.01 | 1.13 ± 0.66 | 0.63 ± 0.18 | 3.76 ± 2.32 | 2.05 ± 0.52 |
| Kohistan–Ladakh batholith | | | | | | |
| Granodiorite | 21 | 1.56 ± 0.73 | 9.31 ± 4.34 | 2.60 ± 0.75 | 6.31 ± 2.51 | 1.86 ± 0.52 |
| Diorite | 15 | 1.14 ± 0.61 | 6.60 ± 2.65 | 2.09 ± 0.78 | 6.98 ± 3.85 | 2.29 ± 1.25 |
| Granite | 12 | 2.96 ± 1.01 | 14.10 ± 5.30 | 3.63 ± 0.71 | 5.18 ± 2.32 | 1.33 ± 0.38 |
| Metavolcanics | 4 | 0.63 ± 0.59 | 2.54 ± 1.90 | 1.18 ± 0.90 | 5.43 ± 2.20 | 2.38 ± 2.07 |
| Gneiss | 3 | 2.73 ± 0.50 | 13.54 ± 1.21 | 2.51 ± 0.38 | 5.12 ± 1.32 | 0.93 ± 0.17 |
| Tonalite | 2 | 0.25 ± 0.15 | 2.95 ± 0.92 | 0.65 ± 0.07 | 15.73 ± 13.27 | 3.06 ± 1.59 |
| Leucogranite | 2 | 2.51 ± 0.70 | 12.76 ± 3.85 | 3.81 ± 0.44 | 5.51 ± 3.07 | 1.60 ± 0.62 |
| Amphibolite | 2 | 0.36 ± 0.25 | 2.56 ± 1.44 | 1.02 ± 0.47 | 7.49 ± 1.14 | 3.11 ± 0.83 |
| Pegmatite | 2 | 1.97 ± 1.07 | 7.47 ± 2.08 | 3.21 ± 0.41 | 4.12 ± 1.17 | 1.85 ± 0.79 |
| Gabbro | 1 | 0.60 | 5.08 | 1.51 | 8.53 | 2.53 |
| Karakoram batholith | | | | | | |
| Gneiss | 11 | 4.70 ± 2.60 | 16.47 ± 8.66 | 3.34 ± 1.20 | 3.63 ± 0.95 | 0.93 ± 0.58 |
| Granite | 7 | 15.81 ± 18.10 | 61.32 ± 55.62 | 3.75 ± 1.04 | 7.04 ± 4.04 | 0.85 ± 0.85 |
| Granodiorite | 6 | 5.10 ± 4.05 | 19.15 ± 15.96 | 3.20 ± 1.54 | 5.58 ± 4.66 | 1.13 ± 0.94 |
| Diorite | 4 | 2.05 ± 1.28 | 10.20 ± 3.81 | 2.42 ± 0.49 | 5.94 ± 2.99 | 1.57 ± 1.07 |
| Pegmatite | 5 | 9.96 ± 4.20 | 9.20 ± 5.06 | 4.44 ± 1.71 | 0.93 ± 0.42 | 0.48 ± 0.17 |
| Leucogranite | 3 | 12.11 ± 7.99 | 10.04 ± 2.63 | 3.38 ± 0.47 | 1.18 ± 0.82 | 0.45 ± 0.39 |
| Syenite | 3 | 3.71 ± 0.15 | 11.87 ± 2.53 | 6.92 ± 0.67 | 3.19 ± 0.62 | 1.86 ± 0.11 |
| Schist | 2 | 2.29 ± 1.44 | 10.38 ± 6.51 | 1.97 ± 1.02 | 4.53 ± 0.01 | 0.89 ± 0.12 |

The detector indirectly calculates the concentrations of U–Th–K through gamma decay of their respective daughter elements. The instrument's accuracy is 2%K, 2 ppm U, and 8 ppm Th, while its precision is $K = \pm 0.35\%$, $U = \pm 1.5$ ppm, $Th = \pm 2.6$ ppm (SAIC Exploranium 2006). A complete data set containing details of individual measurements with geographic coordinates is provided in the Additional file 1

the mean Th concentration in KB granites is significantly high (61.32 ± 55.62 ppm) compared to NPM and KLB (20.70 ± 6.36 and 14.10 ± 5.30 ppm, respectively). The highest mean K value is found in the KB syenites ($6.92\% \pm 0.67\%$), surpassing the NPM granites and pegmatites ($4.22\% \pm 0.65\%$ and $3.63\% \pm 0.71\%$, respectively).

Figure 4 shows lithology-based relative concentrations of U, Th, and K in the NPM, KLB, and KB. In the NPM, gneisses differ from granites and pegmatites with a higher Th proportion (>0.6 in most samples), while the granites, pegmatite, and some gneisses have slightly higher U proportion (~ 0.4 – 0.5). The relative K content is higher in pegmatite than in the other rocks (Fig. 4a). In contrast, the relative Th and U contents in most KLB rocks show minor variability (Fig. 4b). The KB rocks display the most variable relative distribution of U, Th, and K contents, with a dominant Th proportion (>0.7) in granites and a dominant U proportion (~ 0.5) in pegmatites and leucogranites. The relative K proportion in syenites and pegmatites is higher than in other lithologies (Fig. 4c).

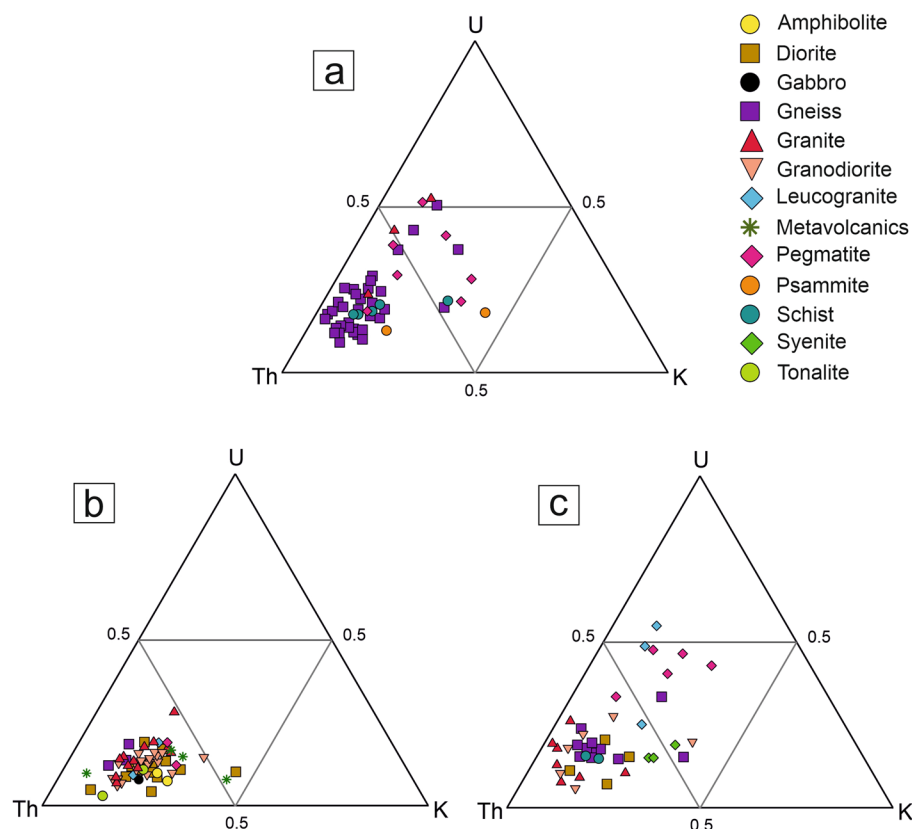


Fig. 4 Ternary plots showing relative concentrations of U (ppm), Th (ppm) and K (wt %) within different lithologies: **(a)** Nanga Parbat Massif comprises Proterozoic basement gneisses (and schists) intruded by recent pegmatite and granites. **b** Kohistan-Ladakh batholith is composed of Cretaceous granitoids and volcanic rocks with Tertiary pegmatitic leucogranites. **c** Karakoram batholith represent Cretaceous and Tertiary granitoids with Proterozoic and Jurassic gneisses

Plots of U vs. Th, U vs. K, and Th vs. K for individual rock samples from the three domains show distinct correlations between radioelements for different lithologies (Fig. 5). The granites and pegmatites of NPM have Th/U ratios ~ 1 , while most gneisses and schists have ratios > 3 (Fig. 5a). In contrast, the Th/U ratio is slightly higher than 3 in most lithologies of KLB, with positive linear correlations between U, Th, and K concentrations (Fig. 5b). U and Th show large variability compared to K in KB granites with distinctly higher Th/U ratio (≥ 5), in contrast to the younger leucogranites and pegmatites with Th/U < 1 . The syenites do not show any correlation of Th and U with K (Fig. 5c).

Radiogenic heat production

The lithologicalwise distribution of minimum and maximum radiogenic heat production values, along with their mean, median, and standard deviations for NPM, KLB, and KB, are presented in Table 2. The radiogenic heat production data from the study area shows an overall variation from 0.1 to 20.3 μWm^{-3} with a mean and median of 2.8 and 1.9 μWm^{-3} , respectively. Based on tectonic affinity, the rocks of the NPM stand out from the rest with a mean of $4.0 \pm 2.5 \mu\text{Wm}^{-3}$ (median 3.9 μWm^{-3}) as compared to the KLB and KB with means of 1.2 ± 0.6 and $3.6 \pm 4.1 \mu\text{Wm}^{-3}$, respectively, indicating that

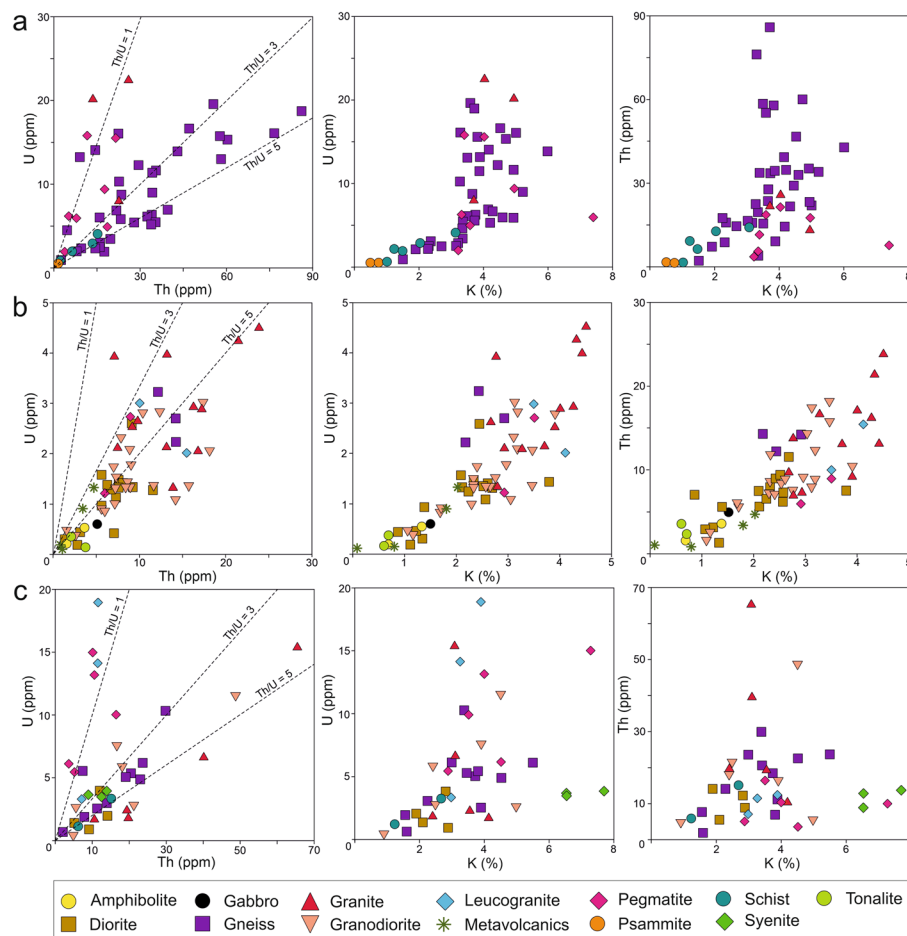


Fig. 5 Plot of U vs. Th and K, and Th vs. K for different rock types in the study area inferred from in-situ gamma spectrometry **(a)** Nanga Parbat Massif, **(b)** Kohistan–Ladakh batholith, **(c)** Karakoram batholith. Note: due to very high U (15.45 and 44.51 ppm) and Th (120.00 and 154.00 ppm) concentrations, two granite samples (from KB) plot outside the selected range in Fig. 5c

the tectonic affinity of rocks is the most significant factor controlling radiogenic heat production.

The NPM comprises Proterozoic basement gneisses with Tertiary granitic and pegmatitic intrusions. Radiogenic heat production values from 53 locations vary from a maximum of 10.8 to $0.2 \mu\text{Wm}^{-3}$. The granites and gneisses show high heat production (mean 4.6 ± 2.5 and $5.9 \pm 1.9 \mu\text{Wm}^{-3}$, respectively), while schists and psammites have low mean values (1.4 ± 1.3 and $0.2 \pm 0.1 \mu\text{Wm}^{-3}$, respectively) (Fig. 6a). The heat production in pegmatites varies between 1.0 and $5.6 \mu\text{Wm}^{-3}$ with a mean of $3.3 \pm 1.6 \mu\text{Wm}^{-3}$.

The KLB consists of various plutonic to volcanic units of the Cretaceous period with felsic to mafic composition with minor Tertiary intrusions. In KLB, the granites, granodiorites, gneisses, leucogranite, and pegmatites display higher mean values (2.0 ± 0.5 , 1.2 ± 0.4 , 1.8 ± 0.1 , 1.8 ± 0.1 , and $1.2 \pm 0.4 \mu\text{Wm}^{-3}$, respectively) than amphibolites, tonalites and metavolcanics (0.3 ± 0.2 , 0.3 ± 0.1 , and $0.4 \pm 0.1 \mu\text{Wm}^{-3}$, respectively) (Fig. 6b). The heat production values in diorites vary between 0.3 and $1.5 \mu\text{Wm}^{-3}$ with a mean of $0.9 \pm 0.3 \mu\text{Wm}^{-3}$.

Table 2 Statistical overview of radiogenic heat production (μWm^{-3}) and density for lithologies within Nanga Parbat Massif, Kohistan–Ladakh, and Karakoram batholiths

| Lithology | N | Density (g cm^{-3}) | Min | Max | Mean | Median | SD \pm |
|---------------------------|----|-------------------------------|------|-------|------|--------|----------|
| Nanga Parbat Massif | | | | | | | |
| Gneiss | 36 | 2.66 | 0.52 | 10.80 | 4.64 | 4.19 | 2.59 |
| Pegmatite | 7 | 2.63 | 1.03 | 5.63 | 3.33 | 2.84 | 1.61 |
| Schist | 5 | 2.76 | 0.37 | 2.39 | 1.43 | 1.33 | 0.75 |
| Granite | 3 | 2.61 | 3.84 | 7.62 | 5.96 | 6.42 | 1.92 |
| Psammite | 2 | 2.70 | 0.20 | 0.24 | 0.22 | – | 0.03 |
| Kohistan–Ladakh batholith | | | | | | | |
| Granodiorite | 21 | 2.65 | 0.32 | 2.22 | 1.26 | 1.17 | 0.49 |
| Diorite | 15 | 2.75 | 0.30 | 1.55 | 0.96 | 1.04 | 0.37 |
| Granite | 12 | 2.62 | 1.29 | 3.18 | 2.02 | 1.85 | 0.57 |
| Metavolcanics | 4 | 2.80 | 0.12 | 0.86 | 0.45 | 0.41 | 0.35 |
| Gneiss | 3 | 2.70 | 1.77 | 1.95 | 1.87 | 1.90 | 0.09 |
| Pegmatite | 2 | 2.69 | 0.97 | 1.60 | 1.28 | – | 0.44 |
| Leucogranite | 2 | 2.60 | 1.73 | 1.90 | 1.82 | – | 0.12 |
| Tonalite | 2 | 2.80 | 0.32 | 0.34 | 0.33 | – | 0.01 |
| Amphibolite | 2 | 2.62 | 0.23 | 0.53 | 0.38 | – | 0.21 |
| Gabbro | 1 | 2.84 | 0.68 | 0.68 | – | – | – |
| Karakoram batholith | | | | | | | |
| Gneiss | 11 | 2.65 | 0.42 | 4.92 | 2.61 | 2.89 | 1.25 |
| Granite | 7 | 2.63 | 1.53 | 20.35 | 8.47 | 4.66 | 8.31 |
| Granodiorite | 6 | 2.65 | 0.49 | 6.50 | 2.87 | 2.67 | 2.05 |
| Pegmatite | 5 | 2.72 | 1.95 | 5.03 | 3.46 | 3.86 | 1.34 |
| Diorite | 4 | 2.59 | 0.92 | 2.12 | 1.47 | 1.42 | 0.53 |
| Leucogranite | 3 | 2.62 | 1.56 | 5.85 | 4.00 | 4.59 | 2.20 |
| Syenite | 3 | 2.58 | 2.08 | 2.57 | 2.32 | 2.31 | 0.24 |
| Schist | 2 | 2.7 | 0.84 | 2.14 | 1.49 | – | 0.92 |

Lowest and highest values are referred as min and max, respectively

SD Standard deviation

The typical lithologies in the KB from which we have collected our data include Proterozoic and Jurassic gneisses, Cretaceous diorites and granodiorites, and Tertiary granites, leucogranites, and pegmatites. Granites display a wide range of radiogenic heat production values, with a maximum value of $20.3 \mu\text{Wm}^{-3}$ and a highest mean of $8.4 \pm 8.3 \mu\text{Wm}^{-3}$ (Fig. 6c). After granites, leucogranites and pegmatite show higher mean values (4.0 ± 2.2 and $3.4 \pm 1.3 \mu\text{Wm}^{-3}$, respectively) compared to gneisses, granodiorites, and syenites, while the diorites and schists show lower heat production (Fig. 6c).

Spatial distribution and classification

Rocks exposed across the entire region exhibit a wide range of radiogenic heat production values due to variability in concentrations of radioelements. These variations can be controlled by various factors, such as petrogenesis, age, rock type, and metamorphism (Artemieva et al. 2017; Jaupart and Mareschal 2005). In this regard, we use the geographic locations of our sampling points to identify and understand these spatial variations within NPM, KLB, and KB (Fig. 7). The concentrations of U and Th within the NPM are primarily high, with the highest values in the core (mostly orthogneiss) while

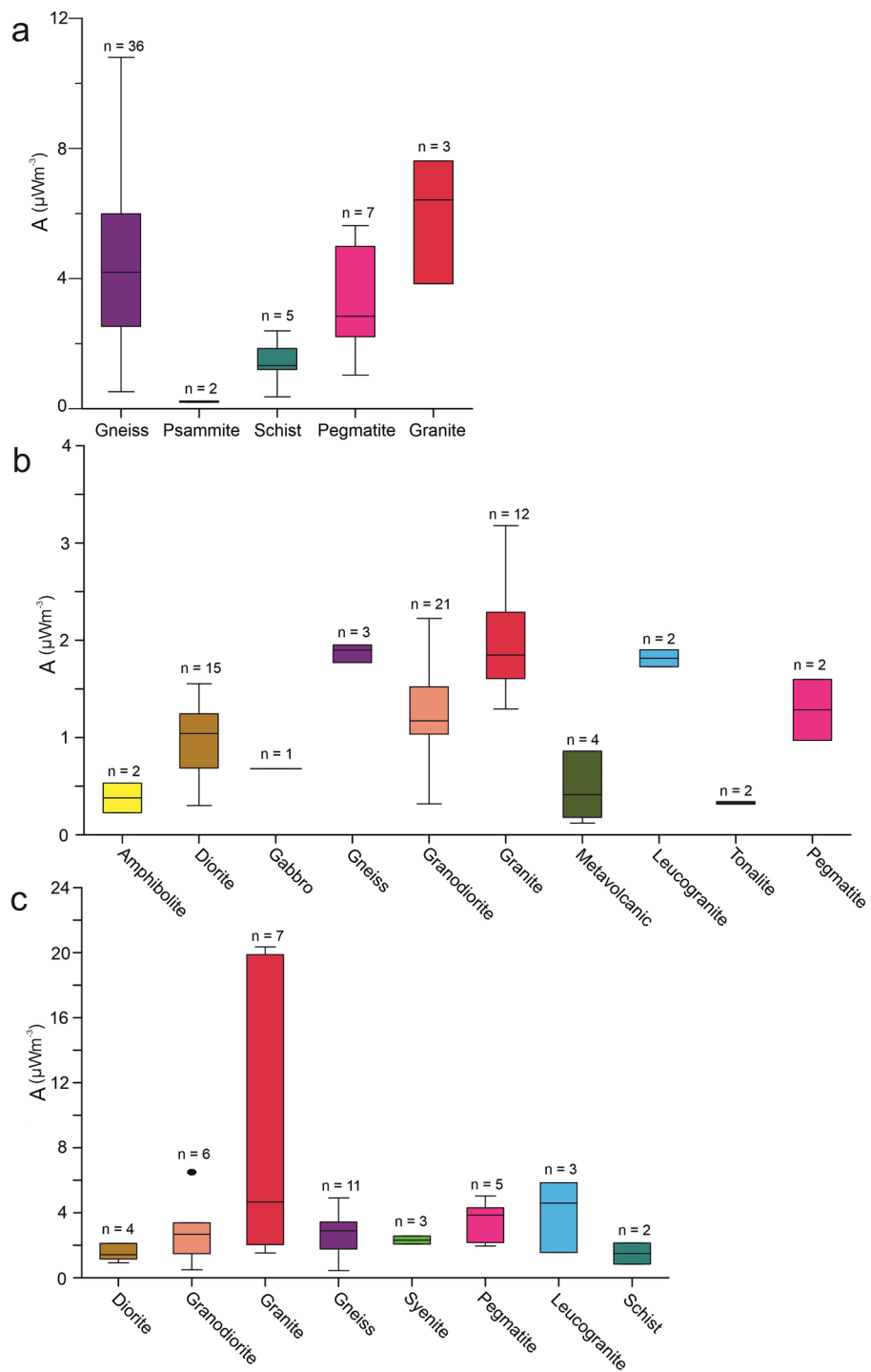


Fig. 6 Lithologywise variations in radiogenic heat production (μWm^{-3}) in the study area (a) Nanga Parbat Massif, (b) Kohistan-Ladakh batholith, (c) Karakoram batholith

decreasing towards the flanks (mostly paragneiss). Values of K are higher in the west and gradually decrease eastward. U and Th in KLB are mostly (low compared to NPM and KB), with a slight increase in felsic units. In KB, high U and Th concentrations in the east

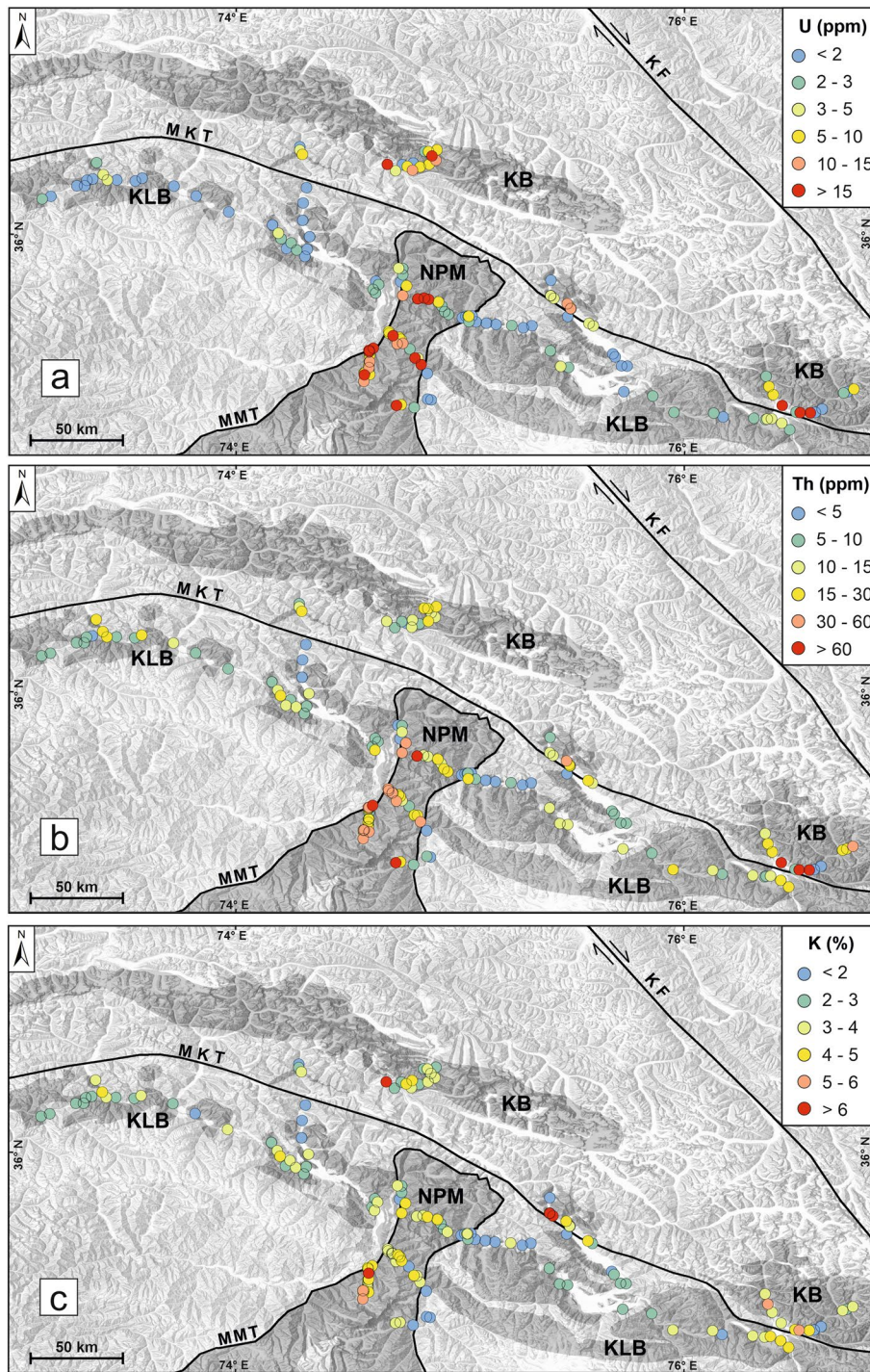


Fig. 7 Spatial distribution of concentrations of radiogenic elements at each spot in the study area. **a** Concentrations of U (in ppm). **b** Concentrations of Th (in ppm). **c** Concentrations of K (in %). Abbreviations are the same as in Fig. 1

are associated with granites (containing hornblende). The syenites and pegmatites from the Shigar and Hunza valleys have high K concentrations, respectively.

There are many classification schemes available for radiogenic heat production values, but they lack a consensus on the thresholds, and each one has established its thresholds depending on data and study area (Carson and Pittard 2012; Gillespie et al. 2013; Huston et al. 2010; McCay and Younger 2017; Siegel et al. 2012). For our study, we have classified radiogenic heat production into six classes, i.e., very low ($< 1 \mu\text{Wm}^{-3}$), low ($1-2 \mu\text{Wm}^{-3}$), moderate ($2-4 \mu\text{Wm}^{-3}$), moderately high ($4-6 \mu\text{Wm}^{-3}$), high ($6-8 \mu\text{Wm}^{-3}$) and very high ($> 8 \mu\text{Wm}^{-3}$).

In the NPM, most locations are moderately high to very high heat producing with few moderate and low values towards the northeast. Most of the sites in KLB are low heat producing with very low values ($< 1 \mu\text{Wm}^{-3}$), mainly associated with outcrops north of Gilgit, along the Astore valley, and in the west of Skardu. There are a few scattered localities with moderate values in granite located east of Khaplu and in Ghizer Valley.

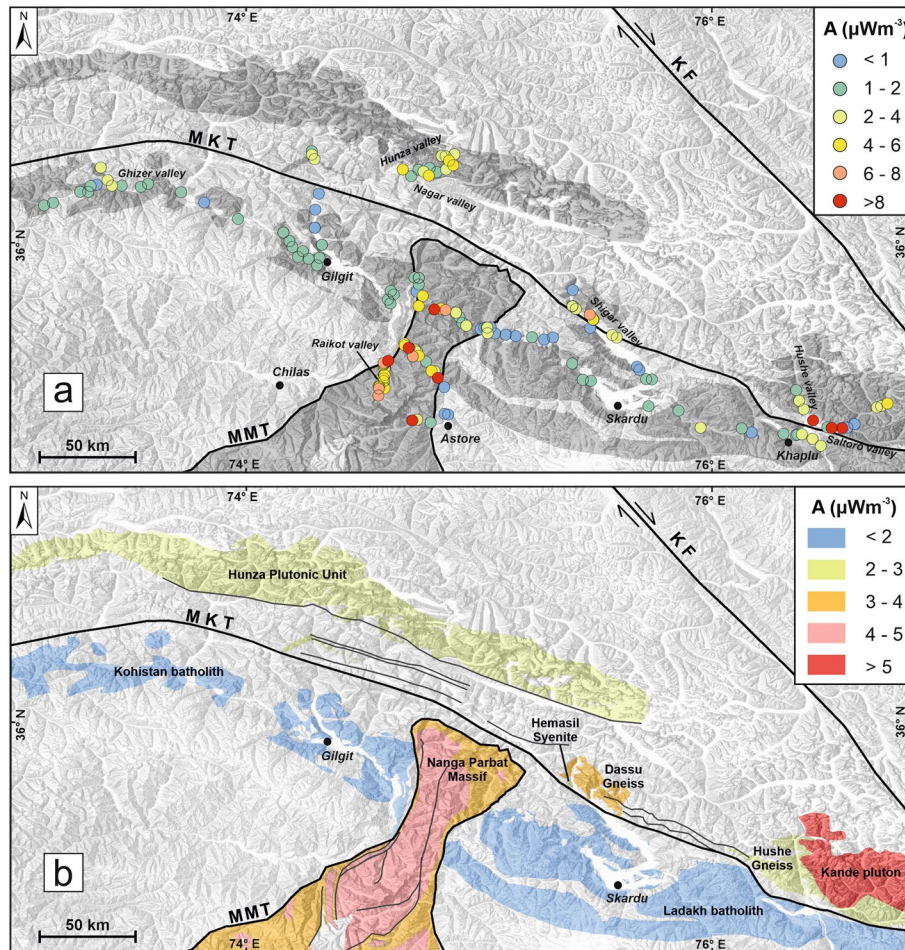


Fig. 8 **a** Radiogenic heat production (μWm^{-3}) for each sample in the Nanga Parbat Massif, Karakoram, and Kohistan–Ladakh batholiths. **b** Mean values of radiogenic heat production (μWm^{-3}) for the different (litho-) tectonic granitoid units in the study area. Weighted mean values are calculated from approximate lithological proportions for Nanga Parbat Massif (after Madin 1986) and Kohistan batholith (after Jagoutz and Schmidt 2012). Simple mean values are used for lithological units of Karakoram (after Khan Searle and Khan 1996)

KB is moderate to moderately high heat producing, with some locations in the Shigar and Saltoro valleys classified as high to very high heat producing (Fig. 8a). The estimated weighted means for radiogenic heat production in NPM and KLB are 4.1 ± 2.0 and $1.0 \pm 0.3 \mu\text{Wm}^{-3}$, respectively. For KB, the Kande pluton has the highest mean value of $7.4 \pm 8.2 \mu\text{Wm}^{-3}$, followed by Dassu gneiss, Hunza plutonic unit, Hemasil syenite, and Hushe gneiss in decreasing order (Fig. 8b).

Discussion

Variations in radioelement concentrations

Lithological variations are mainly responsible for the heterogeneous distribution of radioelement concentrations, which control the crustal heat production and tend to increase in rocks with felsic (SiO_2 abundant) composition (Jaupart and Mareschal 2005; Kukkonen and Lahtinen 2001). Radiogenic heat production depends directly upon concentrations of U, Th, and K in decreasing order (Rybach 1988); therefore, rocks with minerals hosting these elements control its magnitude. Few studies suggested a negative correlation between radiogenic heat production, age, and metamorphism grade (McLaren et al. 2003; Vilà et al. 2010). However, the tectonic origin, setting, and chemical composition play more significant roles in controlling the radioelement concentration and heat production than the geological age (Kemp and Hawkesworth 2003). Our results indicate that granite, leucogranite, gneiss (pelitic and granitic), and pegmatite have a higher concentration of U, Th, K, and subsequent higher radiogenic heat productions than intermediate and mafic rocks, such as granodiorite, tonalite, diorite, gabbro, and metavolcanics (Table 1). Commonly, in granites, K is abundant in alkali feldspars (orthoclase and microcline) and micas (muscovite); therefore, its concentration is naturally high in alkali–granite, syenite, and leucogranite. e.g., the Hemasil syenite in the Shigar Valley has the highest potassium concentration (>6 wt %). U and Th commonly occur in accessory minerals (such as zircon, monazite, xenotime, apatite, and allanite), and peraluminous granitoids tend to be abundant in such minerals (Bea 1996). The granitoids of the KLB and KB (except Tertiary granitic intrusions) are mostly metaluminous I-type, and, therefore, have lower concentrations of U and Th than the peraluminous S-type Tertiary granitoids of the NPM and KB (Kande pluton).

We also see a significant role of genetic association, which is controlling the concentrations of radioelements. For example, the gneisses of NPM show enrichment in radioelements compared to the ones of KLB and KB. The NPM, suggested as a metamorphosed and evolved component of the Indian continental crust (Butler 2019; Treloar et al. 2019), shows similar radioelement signatures with the Besham complex as well as central and southern Indian shield rocks (Ahmad et al. 2021; Kumar et al. 2009; Ray et al. 2008, 2016). Such a widespread phenomenon has been observed globally in early to middle Proterozoic granitoids, which is attributed to large-scale orogenic and magmatic processes involving mantle plumes related to the assembling of continents before the formation of the supercontinent Nuna (Columbia) (Artemieva et al. 2017; Spencer et al. 2018).

The concentrations of incompatible radioelements (U and Th) can be affected by remobilization due to dehydration and fluid flow during metamorphism and partial melting, leading to their enrichment in leucogranites, pegmatites, and granites compared to their parent rocks. The average crustal ratios of Th/U and K/U are 4 and 1×10^4 ,

respectively (Taylor and McLennan 1985; Jochum et al. 1983). Uranium is relatively more mobile compared to Thorium (Scott et al. 1992), due to which we see U enrichment in Tertiary intrusions of NPM and KB (leucogranite and pegmatite), resulting in low Th/U and K/U (~ 1 and $< 0.5 \times 10^4$, respectively). By contrast, the Th/U ratio > 3 in the granite form KLB does not indicate mobilization of U. The granites from Kande pluton of KB with the highest concentration of radioelements suggest enrichment in localized zones and require further detailed investigations. At the same time, high Th/U ratios in these granites are > 4 , suggesting Th enrichment and possibly indicating a deep crustal source distinguishing them from anatectic Himalayan leucogranites (Mahar et al. 2014; Searle et al. 2010).

Effect of radiogenic heat production on crustal geotherms

According to McCay and Younger (2017), the near-surface presence of rock units with high heat production ($> 4 \mu\text{Wm}^{-3}$) and large volume can generate enough heat to raise the geothermal gradients significantly. Our results identify gneisses in the NPM and granites in the eastern KB as high heat producing. Though these granites (of KB) have the highest mean heat production $8.4 \pm 8.3 \mu\text{Wm}^{-3}$, their high standard deviation suggests localized highly enriched zones of radioelements rather than a uniform distribution (Searle et al. 1992). On the other hand, NPM's gneisses (with paragneiss and orthogneiss units) have mean heat production of $4.6 \pm 2.5 \mu\text{Wm}^{-3}$ with an estimated exposed thickness of about 8 km, respectively (Madin et al. 1989). The granites (in NPM) have a small volume ($< 20\%$; Madin et al. 1989), but due to high heat production of $5.9 \pm 1.9 \mu\text{Wm}^{-3}$ can also induce localized thermal impulses.

To model the effect of this high heat production on near-surface crustal geotherms, we took NPM as an end-member example and performed 1D steady-state modeling using a finite-difference solution for the conductive heat transfer equation with heat sources. There is a general agreement in the literature over a decreasing trend in heat production with depth (Jaupart et al. 2016 and references therein). However, the vertical and horizontal heterogeneity, especially in the upper crust, hinders putting stratigraphic control on the heat production distribution (Vilà et al. 2010). A possible solution is assuming multiple scenarios with variable thicknesses (5, 10, and 15 km) of a heat-producing layer (HPL) of $4 \mu\text{Wm}^{-3}$ (as the weighted mean of NPM) to estimate crustal (mainly upper crustal) temperature ranges. For a lower boundary condition, some studies have used Moho heat flow to model crustal geotherms over parts of the Indian craton (Kumar et al. 2007; 2009). However, due to the thicker lithosphere and dynamic orogenic setting of our study area, we took the lithosphere–asthenosphere boundary as the base of our model. Based on available estimates, a 70 km thick crust with a variably 150–250 km thick continental lithosphere was assumed to accommodate its dynamic uncertainty (Li and Mashele 2009; Kumar et al. 2022; Jadoon et al. 2021). The crust is assumed to consist of a 25 km thick upper crust (including HPL) and a 45 km thick lower crust. Standard heat production values of 0.02, 0.4, and $2 \mu\text{Wm}^{-3}$ are taken for the mantle lithosphere, lower crust, and upper crust, respectively (Hasterok and Chapman 2011). The temperature at the upper boundary is assumed to be 10°C and 1300°C at the lower boundary (McKenzie et al. 2005).

Temperature-dependent thermal conductivity and radiative heat transfer were also incorporated into the modeling (Jaupart et al. 2016; Jaupart and Mareschal 2005).

Our modeling indicates that for the upper crust, a change of 10 km in the thickness of HPL significantly affects the geotherms in contrast to a 100 km change in lithospheric thickness (Fig. 9). The calculated temperatures (with 200 km lithosphere) for the three HPL cases show variations ranging from 337 to 430 °C at 10 km further increasing between 578 and 686 °C at 20 km. Similarly, the heat flow calculated at the surface is 84, 94, and 103 mW m⁻² for HPL of 5, 10, and 15 km thick, respectively. This estimate gives an initial indication that in the case of crustal thickening, a thickened HPL significantly increases upper crustal temperatures even close to partial melting conditions. While our model does not explore the recent dynamic conditions (exhumation and anatexis) at NPM, this static and conductive model still accounts for the relative effect of thick HPL. It also provides an insight into the potential role of heat production, which could have created a hot and weak crust, possibly leading to NPM exhumation upon extrusion (Guevara et al. 2022).

Implications on regional geothermal systems

The hydrothermal activity in the region generally manifests in the form of hot springs and alteration zones, mainly along the faults (Zaigham et al. 2009). Our study area's complex geodynamic and tectonic setting implies that multiple factors could control the heat flow and the geothermal gradient. While frictional heating is restricted to the perimeter of fault zones (Ai et al. 2021), rocks enriched in radioelements occur widely and could strongly affect geothermal gradient and surface heat flow (Jaupart et al. 2016; Pinet and Jaupart 1987). In addition, exhumation and denudation can rapidly exhume hot rocks to the surface and thus create a high near-surface geothermal gradient (Chamberlain et al. 2002; Zeitler et al. 2001).

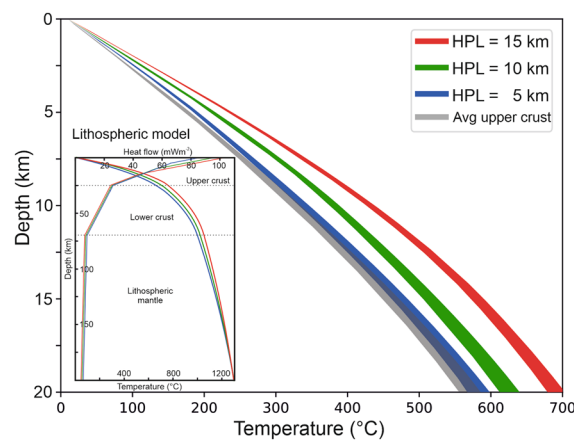


Fig. 9 1D steady-state conductive geotherms show the effect of the heat-producing layer ($4 \mu\text{Wm}^{-3}$) with three cases of increasing thicknesses (red, green, and blue) in the upper crust. The grey curve represents the average felsic upper crust with $2 \mu\text{Wm}^{-3}$ heat production. The thick curves represent (slight) variations in temperature with varying lithospheric thickness from 150 to 250 km. The inset figure shows the 1D thermal model for a 200 km thick lithosphere. Heat flow curves in the inset figure (bottom left to upper right) display an increase in surface heat flow with increasing thickness of the heat-producing layer (from 5 to 15 km)

The steaming geysers in NPM are believed to result of a high geothermal gradient created by the rapid tectonic uplift and young intrusions (Craw et al. 1997). Seismic and magnetotelluric studies have suggested a hot, weak crust that can generate partial melts upon decompression during uplift (Crowley et al. 2009; Meltzer et al. 2001; Park and Mackie 2000). Although the rapid advection of hot “dry” rocks to the surface causing elevation of isotherms has been suggested to be the heat source for the geothermal system (Chamberlain et al. 2002), our conductive model with 187–235 °C at 5 km suggests a significant additional contribution from radiogenic heat production, thus increasing the overall geothermal gradient.

The spatial proximity of hot springs to high heat-producing regions in the study area indicates hydrothermal fluid circulation in zones with enhanced geothermal gradients. These hot springs, commonly bounded to zones of enhanced permeability (such as faults), are likely to tap the proximal zones of increased heat production efficiently. Furthermore, in contrast to conduction, the interaction of topographic-driven deep groundwater flow with heat-producing hot rocks results in advective heat transport to the surface, which is more efficient and rapid near-surface heat transport process common in evolving orogens (Chamberlain et al. 1995; Wanner et al. 2020).

Conclusion

The study provides the first data set of radiogenic heat production of different lithological units in the Western Himalaya, Kohistan, and Karakoram regions of northern Pakistan. The radio-elemental concentrations in Nanga Parbat Massif are overall high (especially granites and gneisses), low in Kohistan–Ladakh batholith (but slightly higher in felsic lithologies) while intermediate in Karakoram batholith (except eastern granites). The distinct radioelemental variations can be explained by the lithological and genetic association of rocks. High radioelement concentrations in the Nanga Parbat Massif are inherited from protoliths, which, upon partial melting, lead to U enrichment (Th/U ratio < 1) in granites and leucogranites. The high radiogenic heat production and Th in Proterozoic gneisses can be attributed to global paleo-tectonic crust-forming processes at that time. Overall, we classify the Nanga Parbat Massif (with $> 4 \mu\text{Wm}^{-3}$) as high heat producing, the Karakoram batholith (with $2\text{--}4 \mu\text{Wm}^{-3}$) as moderately heat-producing, and the Kohistan–Ladakh batholith (with $< 2 \mu\text{Wm}^{-3}$) as low heat-producing.

The thick heat-producing layer in the upper crust can significantly increase the crustal temperatures, leading to overall upwelling of geotherms. The proximity of locations to high radiogenic heat production to the hot springs suggests its potential contribution towards the geothermal gradients in the study area on a local to regional scale. Such thermally enhanced regions warrant detailed investigations to establish their geothermal potential.

Supplementary Information

The online version contains supplementary material available at <https://doi.org/10.1186/s40517-023-00273-3>.

Additional file 1. Supplementary data showing the gamma spectrometry measurements with geographical coordinates and geological information. Radiogenic heat production (A) values are calculated after applying geometric, topographic, and U-disequilibrium corrections to the data.

Acknowledgements

István Dunkl (Georg-August University of Göttingen) is exclusively thanked for lending the gamma spectrometer for fieldwork in Pakistan. The authors thank Humaad Ghani (Georg-August University of Göttingen) for providing valuable insights into improving the manuscript and illustrations. The authors are also grateful to Javed Akhter (Karakorum International University), Shehryar Sattar, Zakaria Hussain, and numerous locals for their kind support during fieldwork. The contribution of two anonymous reviewers towards improvement in the quality of the manuscript is gratefully acknowledged.

Author contributions

Conceptualization: MA and BW. Methodology: MA, JK, BL and DH. Data collection: MA and MMS. Modeling: DH and EL. Visualization: MA and AAW. Supervision: JK, BL, BW and MMS. Writing—original draft: MA and JK. Writing—review and editing: MA, JK, BL, DH, AAW, BW, MMS, and EL.

Funding

Open Access funding enabled and organized by Projekt DEAL. This study is funded through a doctoral fellowship by the DAAD—Deutscher Akademischer Austauschdienst (MA) through the German Federal Ministry of Education. The project also received funding from the DFG—Deutsche Forschungsgemeinschaft; Project KL 495/32-1 (JK) and GAUSS—Georg-August University of Göttingen School of Science (MA).

Availability of data and materials

All data generated or analyzed during this study are included in this published article [and its Additional file 1]. The code used for thermal modeling in this paper is available online on Zenodo (<https://doi.org/10.5281/zenodo.7875951>) and on Github (<https://github.com/davidhindle/steady-nl-heat/tree/steady-nl-heat>).

Declarations

Competing interests

The authors declare that they have no competing interests.

Received: 8 October 2022 Accepted: 18 October 2023

Published online: 27 October 2023

References

- Ahmad T, Arif M, Qasim M, Sajid M. Petrology of granitoids from Indus syntaxis, northern Pakistan: implications for paleoproterozoic A-type magmatism in north-western Indian Plate. *Geochemistry*. 2021;81(1):125693.
- Ai Y, Zhang J, Dong M, Wang B, Fang G. Heat generation effects from shear friction along Xianshui river strike-slip fault in Western Sichuan. *China Geothermics*. 2021;89:101936.
- Artemieva IM, Thybo H, Jakobsen K, Sørensen NK, Nielsen LS. Heat production in granitic rocks: global analysis based on a new data compilation GRANITE2017. *Earth Sci Rev*. 2017;172:1–26.
- Bakht MS. An overview of geothermal resources of Pakistan. *Proceedings of the World Geothermal Congress*. Kyushu-Tohoku, Japan; 2000. p. 77–83.
- Bea F. Residence of REE, Y, Th and U in granites and crustal protoliths; implications for the chemistry of crustal melts. *J Petrol*. 1996;37(3):521–52.
- Bertrand J-M, Kienast J-R, Pinardon J-L. Structure and metamorphism of the Karakorum gneisses in the Braldu-Baltoro Valley (North Pakistan). *Geodin Acta*. 1988;2(3):135–50.
- Butler RW. Tectonic evolution of the Himalayan syntaxes: the view from Nanga Parbat. *Geol Soc London Special Pub*. 2019;483(1):215–54.
- Butler RW, Prior DJ. Tectonic controls on the uplift of the Nanga Parbat Massif, Pakistan Himalayas. *Nature*. 1988;333(6170):247–50.
- Butler RW, Prior DJ, Knipe RJ. Neotectonics of the Nanga Parbat syntaxis, Pakistan, and crustal stacking in the Northwest Himalayas. *Earth Planet Sci Lett*. 1989;94(3–4):329–43.
- Butler RW, Harris NB, Whittington AG. Interactions between deformation, magmatism and hydrothermal activity during active crustal thickening: a field example from Nanga Parbat, Pakistan Himalayas. *Mineral Mag*. 1997;61(404):37–52.
- Carson CJ, Pittard M. A reconnaissance crustal heat production assessment of the Australian Antarctic Territory (AAT). Canberra: Geoscience Australia; 2012.
- Chamberlain CP, Zeitler PK, Barnett DE, Winslow D, Poulson SR, Leahy T, et al. Active hydrothermal systems during the recent uplift of Nanga Parbat, Pakistan Himalaya. *J Geophys Res Solid Earth*. 1995;100(B1):439–53.
- Chamberlain CP, Koons PO, Meltzer AS, Park SK, Craw D, Zeitler P, et al. Overview of hydrothermal activity associated with active orogenesis and metamorphism: Nanga Parbat, Pakistan Himalaya. *Am J Sci*. 2002;302(8):726–48.
- Craw D, Koons PO, Winslow D, Chamberlain CP, Zeitler P. Boiling fluids in a region of rapid uplift, Nanga Parbat massif, Pakistan. *Earth Planet Sci Lett*. 1994;128(3–4):169–82.
- Craw D, Chamberlain CP, Zeitler PK, Koons PO. Geochemistry of a dry steam geothermal zone formed during rapid uplift of Nanga Parbat, northern Pakistan. *Chem Geol*. 1997;142(1–2):11–22.
- Crawford MB, Searle MP. Field relationships and geochemistry of pre-collisional (India-Asia) granitoid magmatism in the central Karakoram, northern Pakistan. *Tectonophysics*. 1992;206(1–2):171–92.
- Crowley JL, Waters DJ, Searle MP, Bowring SA. Pleistocene melting and rapid exhumation of the Nanga Parbat massif, Pakistan: age and P-T conditions of accessory mineral growth in migmatite and leucogranite. *Earth Planet Sci Lett*. 2009;288(3–4):408–20.

- Debon F, Le Fort P, Dautel D, Sonet J, Zimmermann JL. Granites of western Karakorum and northern Kohistan (Pakistan): a composite Mid-Cretaceous to upper Cenozoic magmatism. *Lithos*. 1987;20(1):19–40.
- Dickson B. Radium isotopes in saline seepages, south-western Yilgarn, Western Australia. *Geochim Et Cosmochim Acta*. 1985;49(2):361–8.
- DIN 52102. Determination of absolute density, dry density, compactness and porosity of natural stone and mineral aggregates German Standard DIN. Berlin: Deutsches Institut für Normung; 1988.
- Erdi-Krausz G, Matolin M, Minty B, Nicolet JP, Reford WS, Schetselaar EM. Guidelines for radioelement mapping using gamma ray spectrometry data. Vienna: International Atomic Energy Agency (IAEA); 2003.
- Exploranium SAIC. Exploranium GR-135G plus the identifier system manual, revision 1.0. Canada: SAIC; 2006.
- Gansser A. The significance of the Himalayan suture zone. *Tectonophysics*. 1980;62(1–2):37–52.
- Gillespie MR, Crane EJ, Barron HF. Deep geothermal energy potential in Scotland. Nottingham: British Geological Survey; 2013.
- Gnojek I, Sedlak J, Rappich V, Skacelova Z, Mlcoch B, Krentz O, et al. Structure of the carboniferous altenberg-teplce caldera (Eastern part of the Krusne hory/Erzgebirge Mts.) revealed by combined airborne and ground gamma-ray spectrometry. *J Geosci*. 2018;63(1):3–20.
- Guevara VE, Smye AJ, Caddick MJ, Searle MP, Olsen T, Whalen L, et al. A modern pulse of ultrafast exhumation and diachronous crustal melting in the Nanga Parbat Massif. *Sci Adv*. 2022;8(31):2689.
- Hasterok D, Chapman DS. Heat production and geotherms for the continental lithosphere. *Earth Planet Sci Lett*. 2011;307(1–2):59–70.
- Hindle D, Besson O. A corrected finite-difference scheme for the flexure equation with abrupt changes in coefficient. *Solid Earth*. 2023;14(2):197–212.
- Hochstein MP, Regenauer-Lieb K. Heat generation associated with collision of two plates: the Himalayan geothermal belt. *J Volcanol Geotherm Res*. 1998;83(1):75–92.
- Huston DL, Ayling B, Connolly D, Huston DL, Lewis B, Mernagh TP, et al. An assessment of the uranium and geothermal potential of north Queensland. Symonston: Geoscience Australia; 2010.
- IAEA. Airborne gamma ray spectrometer surveying; technical reports series No. 323. Vienna: International Atomic Energy Agency; 1991.
- Jadoon IAK, Ding L, Jadoon ur RKS, Bhatti ZI, Shah STH, Qasim M. 2021 Lithospheric deformation and active tectonics of the NW Himalayas, Hindukush, and Tibet. *Lithosphere*. 2021;1:7866954.
- Jagoutz O, Schmidt MW. The formation and bulk composition of modern juvenile continental crust: the Kohistan arc. *Chem Geol*. 2012;298:79–96.
- Jaupart C, Mareschal JC. Constraints on crustal heat production from heat flow data. In: Holland HD, Turekian KK, editors. *The crust treatise on geochemistry*. Oxford: Elsevier-Pergamon; 2005.
- Jaupart C, Mareschal J-C, Iarotsky L. Radiogenic heat production in the continental crust. *Lithos*. 2016;1(262):398–427.
- Jochum KP, Hofmann AW, Ito E, Seufert HM, White WM, U K. , and Th in mid-ocean ridge basalt glasses and heat production, K/U and K/Rb in the mantle. *Nature*. 1983;306(5942):431–6.
- Kazmi AH, Jan MQ. *Geology and tectonics of Pakistan*. Karachi: Graphic publishers; 1997. p. 554.
- Kazmi AH, Lawrance RD, Dawood H, Snee LW, Hussain SS. Geology of The indus suture zone in the Mingora-Swat Shangla area of Swat, N Pakistan. *J Himal Earth Sci*. 1984;17:127–144.
- Kemp AIS, Hawkesworth CJ. Granitic perspectives on the generation and secular evolution of the continental crust. In: Holland HD, editor. *Treatise on geochemistry*. Amsterdam: Elsevier; 2003.
- Kukkonen IT, Lahtinen R. Variation of radiogenic heat production rate in 2.8–1.8 Ga old rocks in the central fennoscandian shield. *Phys Earth Planet Inter*. 2001;126(3–4):279–94.
- Kumar PS, Menon R, Reddy GK. The role of radiogenic heat production in the thermal evolution of a Proterozoic granulite-facies orogenic belt: Eastern Ghats, Indian Shield. *Earth Planet Sci Lett*. 2007;254(1–2):39–54.
- Kumar PS, Menon R, Reddy GK. Heat production heterogeneity of the Indian crust beneath the Himalaya: Insights from the northern Indian Shield. *Earth Planet Sci Lett*. 2009;283(1–4):190–6.
- Kumar V, Rai SS, Hawkins R, Bodin T. Seismic imaging of crust beneath the western Tibet-Pamir and Western Himalaya using Ambient Noise and Earthquake Data. *J Geophys Res Solid Earth*. 2022. <https://doi.org/10.1029/2021JB022574>.
- Li A, Mashele B. Crustal structure in the Pakistan Himalaya from teleseismic receiver functions. *Geochem Geophys Geosyst*. 2009. <https://doi.org/10.1029/2009GC002700>.
- Madin IP. Structure and neotectonics of the northwestern Nanga Parbat-Haramosh massif. Corvallis: Oregon State University; 1986.
- Madin IP, Lawrence RD, Ur-Rehman S. The northwestern Nanga Parbat-Haramosh Massif; Evidence for crustal uplift at the northwestern corner of the Indian Craton. In: Malinconico LL, Lillie RJ, editors. *Tectonics of the western Himalayas*. Boulder: Geological Society of America Special Papers; 1989. p. 169–82.
- Mahar MA, Mahéo G, Goodell PC, Pavlis TL. Age and origin of post collision Baltoro granites, south Karakoram, North Pakistan: insights from in-situ U-Pb, Hf and oxygen isotopic record of zircons. *Lithos*. 2014;205:341–58.
- McCay AT, Younger PL. Ranking the geothermal potential of radiothermal granites in Scotland: are any others as hot as the Cairngorms? *Scott J Geol*. 2017;53(1):1–11.
- McCay AT, Harley TL, Younger PL, Sanderson DC, Cresswell AJ. Gamma-ray spectrometry in geothermal exploration: state of the art techniques. *Energies*. 2014;7(8):4757–80.
- McKenzie D, Jackson J, Priestley K. Thermal structure of oceanic and continental lithosphere. *Earth Planet Sci Lett*. 2005;233(3):337–49.
- McLaren S, Sandiford M, Hand M, Neumann N, Wyborn L, Bastrakova I. The hot southern continent: heat flow and heat production in Australian Proterozoic terranes. In: Hillis RR, Müller RD, editors. *Evolution and dynamics of the Australian Plate*. Geological Society of America; 2003. p. 157–68.
- Meltzer A, Sarker G, Beaudoin B, Seeber L, Armbruster J. Seismic characterization of an active metamorphic massif, Nanga Parbat, Pakistan Himalaya. *Geology*. 2001;29(7):651–4.
- Minty B. Fundamentals of airborne gamma-ray spectrometry. *J Aust Geol Geophys*. 1997;17:39–50.
- Minty B, Wilford J. Radon effects in ground gamma-ray spectrometric surveys. *Explor Geophys*. 2004;35(4):312–8.

- Palin RM, Searle MP, Waters DJ, Horstwood MSA, Parrish RR. Combined thermobarometry and geochronology of peraluminous metapelites from the Karakoram metamorphic complex, North Pakistan; new insight into the tectonothermal evolution of the Baltoro and Hunza Valley regions. *J Metamorph Geol.* 2012;30(8):793–820.
- Park SK, Mackie RL. Resistive (dry?) lower crust in an active orogen, Nanga Parbat, northern Pakistan. *Tectonophysics.* 2000;316(3–4):359–80.
- Petterson MG. A review of the geology and tectonics of the Kohistan island arc, north Pakistan. *Geol Soc Spec Publ.* 2010;338(1):287–327.
- Petterson MG, Treloar PJ. Volcanostratigraphy of arc volcanic sequences in the Kohistan arc, North Pakistan: volcanism within island arc, back-arc-basin, and intra-continental tectonic settings. *J Volcanol Geotherm Res.* 2004;130(1–2):147–78.
- Petterson MG, Windley BF. RbSr dating of the Kohistan arc-batholith in the Trans-Himalaya of north Pakistan, and tectonic implications. *Earth Planet Sci Lett.* 1985;74(1):45–57.
- Petterson MG, Crawford MB, Windley BF. Petrogenetic implications of neodymium isotope data from the Kohistan batholith, North Pakistan. *J Geol Soc.* 1993;150(1):125–9.
- Pinet C, Jaupart C. A thermal model for the distribution in space and time of the Himalayan granites. *Earth Planet Sci Lett.* 1987;84(1):87–99.
- Ray L, Roy S, Srinivasan R. High radiogenic heat production in the Kerala Khondalite block, Southern Granulite province. *India Int J Earth Sci.* 2008;97(2):257–67.
- Ray L, Nagaraju P, Singh SP, Ravi G, Roy S. Radioelemental, petrological and geochemical characterization of the Bundelkhand craton, central India: implication in the Archaean geodynamic evolution. *Int J Earth Sci.* 2016;105:1087–107.
- Reinhardt N, Herrmann L. Gamma-ray spectrometry as versatile tool in soil science: a critical review. *J Plant Nutr Soil Sci.* 2019;182(1):9–27.
- Rybach L. Determination of heat production rate. In: Haenel R, Rybach L, Stegena L, editors. *Handbook of terrestrial heat-flow density determination.* Springer; 1988. p. 9–57.
- Scott RD, MacKenzie AB, Alexander WR. The interpretation of ^{238}U – ^{234}U – ^{230}Th – ^{226}Ra disequilibria produced by rock-water interactions. *J Geochem Explor.* 1992;45(1–3):323–43.
- Searle MP, Khan MA. Geological map of north Pakistan and adjacent areas of northern Ladakh and western Tibet (Western Himalaya, salt ranges, Kohistan, Karakoram, Hindu Kush) Scale 1:650,000. Oxford: Oxford University; 1996.
- Searle MP, Tirrul R. Structural and thermal evolution of the Karakoram crust. *J Geol Soc.* 1991;148(1):65–82.
- Searle MP, Rex AJ, Tirrul R, Rex DC, Barnicoat A, Windley BF. Metamorphic, magmatic, and tectonic evolution of the central Karakoram in the Biafo-Baltoro-Hushe regions of northern Pakistan. In: Malinconico LL Jr, Lillie RJ, editors. *Tectonics of the western Himalayas.* Boulder: Geological Society of America; 1989.
- Searle MP, Crawford MB, Rex AJ. Field relations, geochemistry, origin and emplacement of the Baltoro granite, central Karakoram. *Earth Environ Sci Trans R Soc Edinb.* 1992;83(3):519–38.
- Searle MP, Khan MA, Fraser JE, Gough SJ, Jan MQ. The tectonic evolution of the Kohistan-Karakoram collision belt along the Karakoram Highway transect, north Pakistan. *Tectonics.* 1999;18(6):929–49.
- Searle MP, Parrish RR, Thow AV, Noble SR, Phillips RJ, Waters DJ. Anatomy, age and evolution of a collisional mountain belt: the Baltoro granite batholith and Karakoram Metamorphic complex Pakistan Karakoram. *J Geol Soc.* 2010;167(1):183–202.
- Siegel C, Bryan S, Purdy D, Allen C, Schrank C, Uysal T, et al. Evaluating the role of deep granitic rocks in generating anomalous temperatures in south-west Queensland. In: Geological Survey of Queensland's Digging Deeper 10 Seminar extended abstracts [Queensland Geological Record 2012/14]. Australia.
- Singh B. Geological set up of a part of the Ladakh Granitoid complex, Ladakh Himalaya. *J Himal Geol.* 1993;4(1):57–62.
- Spencer CJ, Murphy JB, Kirkland CL, Liu Y, Mitchell RN. A Palaeoproterozoic tectono-magmatic lull as a potential trigger for the supercontinent cycle. *Nat Geosci.* 2018;11(2):97–101.
- Tahirkheli RK. Geology of Kohistan and adjoining Eurasian and Indo-Pakistan continents, Pakistan. *Geol Bull Univ Peshawar.* 1979;11(1):1–30.
- Tahirkheli RK. Geological evolution of Kohistan island arc on the southern flank of the Karakoram-Hindu Kush in Pakistan. *Bollettino Geofisica Terica Ed Applicata.* 1983;25:351–64.
- Taylor SR, McLennan SM. The continental crust, its composition and evolution: an examination of the geochemical record preserved in sedimentary rocks. Oxford: Blackwell Scientific; 1985.
- Treloar PJ. Thermal controls on early-tertiary, short-lived, rapid regional metamorphism in the NW Himalaya. *Pakistan Tectonophysics.* 1997;273(1–2):77–104.
- Treloar PJ, Brodie KH, Coward MP, Jan MQ, Khan MA, Knipe RJ, et al. The evolution of the Kamila shear zone, Kohistan, Pakistan. In: Salisbury MH, Fountain DM, editors, et al., *Exposed cross-sections of the continental crust.* Dordrecht: Springer; 1990. p. 175–214.
- Treloar PJ, Petterson MG, Jan MQ, Sullivan MA. A re-evaluation of the stratigraphy and evolution of the Kohistan arc sequence, Pakistan Himalaya: implications for magmatic and tectonic arc-building processes. *J Geol Soc.* 1996;153(5):681–93.
- Treloar PJ, Palin RM, Searle MP. Towards resolving the metamorphic enigma of the Indian Plate in the NW Himalaya of Pakistan. *Geol Soc Spec Publ.* 2019;483(1):255–79.
- Vilà M, Fernández M, Jiménez-Munt I. Radiogenic heat production variability of some common lithological groups and its significance to lithospheric thermal modeling. *Tectonophysics.* 2010;490(3–4):152–64.
- Villa IM, Lemennicier Y, Le Fort P. Late miocene to early pliocene tectonometamorphism and cooling in south-central Karakoram and Indus-Tsangpo suture, Chogo Lungma area (NE Pakistan). *Tectonophysics.* 1996;260(1–3):201–14.
- Wanner C, Waber HN, Bucher K. Geochemical evidence for regional and long-term topography-driven groundwater flow in an orogenic crystalline basement (Aar Massif, Switzerland). *J Hydrol.* 2020;581:124374.
- Younis H, Ahmad F, Anees M, Atiq A, Shakeel N, Adil M, et al. Gamma radioactivity and environmental radiation risks of Granitoids in central and Western Gilgit-Baltistan, Himalayas, North Pakistan. *Results Phys.* 2022;37:105509.

- Zaigham NA, Nayyar ZA, Hisamuddin N. Review of geothermal energy resources in Pakistan. *Renew Sustain Energy Rev.* 2009;13(1):223–32.
- Zeitler PK, Sutter JF, Williams IS, Zartman R, Tahirkheli RAK. Geochronology and temperature history of the Nanga Parbat-Haramosh massif, Pakistan. In: Malinconico LL, Lillie RJ, editors. *Tectonics of the western Himalayas*. Geological Society of America; 1989. p. 1–22.
- Zeitler PK, Chamberlain CP, Smith HA. Synchronous anatexis, metamorphism, and rapid denudation at Nanga Parbat (Pakistan Himalaya). *Geology.* 1993;21(4):347–50.
- Zeitler PK, Koons PO, Bishop MP, Chamberlain CP, Craw D, Edwards MA, et al. Crustal reworking at Nanga Parbat, Pakistan: metamorphic consequences of thermal-mechanical coupling facilitated by erosion. *Tectonics.* 2001;20(5):712–28.

Publisher's Note

Springer Nature remains neutral with regard to jurisdictional claims in published maps and institutional affiliations.

Submit your manuscript to a SpringerOpen[®] journal and benefit from:

- ▶ Convenient online submission
- ▶ Rigorous peer review
- ▶ Open access: articles freely available online
- ▶ High visibility within the field
- ▶ Retaining the copyright to your article

Submit your next manuscript at ▶ [springeropen.com](https://www.springeropen.com)
